Emphysema diagnosis using X-ray dark-field imaging at a laser-driven compact synchrotron light source

Simone Schleede[a,1], Felix G. Meinel[b], Martin Bech[a,c], Julia Herzen[a], Klaus Achterhold[a], Guillaume Potdevin[a], Andreas Malecki[a], Silvia Adam-Neumair[d], Sven F. Thieme[b], Fabian Bamberg[b], Konstantin Nikolaou[b], Alexander Bohla[e], Ali Ö. Yildirim[e], Roderick Loewen[f], Martin Gifford[f], Ronald Ruth[g], Oliver Eickelberg[e], Maximilian Reiser[b], and Franz Pfeiffer[a]

[a]Department of Physics and Institute of Medical Engineering, Technische Universität München, 85748 Garching, Germany; [b]Institute for Clinical Radiology, Ludwig-Maximilians-University Hospital Munich, 81377 Munich, Germany; [c]Medical Radiation Physics, Lund University, 22185 Lund, Sweden; [d]Anatomy Department, Ludwig-Maximilians-University Munich, 80336 Munich, Germany; [e]Comprehensive Pneumology Center, Institute of Lung Biology and Disease, Helmholtz Zentrum Munich, 85764 Neuherberg, Germany; [f]Lyncean Technologies, Inc., Palo Alto, CA 94306; and [g]SLAC National Accelerator Laboratory, Menlo Park, CA 94025

Edited by Joe W. Gray, Oregon Health and Science University, Portland, OR, and accepted by the Editorial Board September 20, 2012 (received for review May 7, 2012)

In early stages of various pulmonary diseases, such as emphysema and fibrosis, the change in X-ray attenuation is not detectable with absorption-based radiography. To monitor the morphological changes that the alveoli network undergoes in the progression of these diseases, we propose using the dark-field signal, which is related to small-angle scattering in the sample. Combined with the absorption-based image, the dark-field signal enables better discrimination between healthy and emphysematous lung tissue in a mouse model. All measurements have been performed at 36 keV using a monochromatic laser-driven miniature synchrotron X-ray source (Compact Light Source). In this paper we present grating-based dark-field images of emphysematous vs. healthy lung tissue, where the strong dependence of the dark-field signal on mean alveolar size leads to improved diagnosis of emphysema in lung radiographs.

grating interferometer | pulmonary emphysema | X-ray imaging

Chronic obstructive pulmonary disease (COPD) is one of the leading causes of morbidity and mortality worldwide (1, 2). The disease is characterized by airflow limitation and lung inflammation as a response to noxious particles or gases, resulting in a progressive deterioration in lung function and health-related quality of life (3, 4).

Emphysema is a common component of COPD, in which airway obstruction and aberrant activity of proteolytic enzymes cause irreversible destruction of alveolar walls and enlargement of distal airspaces. Despite this altered lung morphology, emphysema is difficult to detect with conventional radiographic imaging, because the decrease in lung tissue density in emphysema may be too small to be appreciated. Chest X-ray is routinely used to screen patients with suspected COPD for emphysema, although it is known that chest X-rays lack sensitivity in mild to moderate emphysema (5). Currently, screening for and early diagnosis of COPD and emphysema largely relies on spirometric lung function tests (6). Spirometry, however, strongly depends on patients' cooperation and is unable to localize emphysematous changes within the lung. Assessing the regional distribution of pulmonary emphysema is crucial for clinical decision-making regarding lung volume reduction surgery and insertion of endobronchial valves (7, 8). Emphysema imaging has been greatly improved with high-resolution computed tomography (HRCT), but its use is limited by the higher radiation dose applied to the patient (5). Some studies have suggested that MRI may complement CT in the imaging of emphysema (5). However, because MRI is time-consuming, expensive, less available, and prone to breathing artifacts, MRI is currently not established in routine imaging of COPD. Direct assessment of microstructural changes in the alveolar network would be desirable to evaluate disease progression and monitor therapy, but this can currently only be achieved through histopathology, which requires invasive biopsy. Especially in early stages of the disease, identification, precise quantification, and localization of emphysema through grating-based X-ray projection imaging could significantly improve COPD diagnosis and therapy, and avoid the higher radiation exposure associated with CT.

Phase-contrast imaging can significantly increase the visibility of lung tissue in single projections, as demonstrated by several other groups (9–11); it has also been shown to improve the diagnostics of pulmonary diseases (12). Multiple air-tissue interfaces present in the inflated lung result in a high degree of X-ray phase contrast and low absorption contrast. Among the phase-contrast imaging methods available—namely, interferometric methods, propagation-based methods, and analyzer-based methods—the latter two were intensively studied in lung imaging (9, 13, 14).

In propagation-based imaging (PBI), the sample is illuminated by a spatially partially coherent source, which creates a Fresnel diffraction pattern after a certain propagation distance behind the sample. This pattern serves as the so-called edge-enhanced image. Propagation-based methods have been applied to mouse, rat, and rabbit lungs and show a speckled intensity pattern that is attributed to the air-filled alveoli acting as aberrated compound refractive lenses (15). Using a single distance from sample to detector, PBI does not allow for a quantitative analysis of lung projections, due to the a priori assumption of a single-material object composition (16). In addition to a high-brilliance X-ray source, a high-resolution detector is needed to resolve the refraction-induced interference fringes.

In diffraction enhanced imaging (DEI) or analyzer-based imaging (ABI) a perfect crystal analyzer is mounted between the object and the detector. This approach requires a high monochromatic flux, typically from a large-scale synchrotron X-ray source. Reflection from the analyzer crystal only occurs for X-rays in a small angular range meeting the Bragg condition of the crystal. Tilting the crystal while monitoring the intensity in each pixel generates a rocking curve, from which absorption, phase, and small-angle scattering information of the sample can be extracted (17, 18). An application of this technique to mouse lung measurements has been demonstrated by Kitchen et al. (19). The so-called scatter rejection or extinction contrast is produced at only

Author contributions: F.G.M., M.B., J.H., K.A., S.F.T., F.B., K.N., A.Ö.Y., R.L., M.G., R.R., O.E., M.R., and F.P. designed research; S.S., F.G.M., M.B., J.H., K.A., G.P., A.M., S.A.-N., F.B., A.B., R.L., M.G., R.R., and F.P. performed research; S.S., F.G.M., M.B., J.H., S.A.-N., A.B., and A.Ö.Y. analyzed data; and S.S., F.G.M., M.B., J.H., F.B., K.N., R.R., M.R., and F.P. wrote the paper.

Conflict of interest statement: R.R.'s contributions to this publication were as a paid consultant of Lyncean Technologies, Inc. and were not part of his Stanford University duties or responsibilities.

This article is a PNAS Direct Submission. J.W.G. is a guest editor invited by the Editorial Board.

[1]To whom correspondence should be addressed. E-mail: schleede@tum.de.

This article contains supporting information online at www.pnas.org/lookup/suppl/doi:10.1073/pnas.1206684109/-/DCSupplemental.

the peak position of the rocking curve, where the analyzer crystal rejects X-rays from small-angle scattering. With diffraction-enhanced peak images, lung tissue can easily be distinguished from the surrounding soft tissue, leading to an improved discrimination between healthy and diseased lung tissue (12, 20). Comparing single-distance PBI and single rocking-angle DEI of mouse and rabbit lungs indicates that DEI yields images of superior contrast than those for PBI, and both techniques show a significant contrast improvement over conventional absorption radiographs (11). The use of DEI with laboratory sources suffers from low monochromatic flux and the resulting long exposure times, which are not compatible with in vivo imaging applications (21, 22).

Grating-based imaging yields phase and dark-field images that are simultaneously obtained with the conventional attenuation-based X-ray image, thus providing three complementary image modalities that are intrinsically registered. More important, the attenuation, phase, and scattering contributions of the object are clearly separable using this technique. Unlike DEI, the grating-based interferometer supplies a large field of view and has also been shown to work with polychromatic sources and in cone-beam geometry (23–26).

Dark-field image contrast is created through changes in the local scattering power of the sample. It is defined via the decrease in visibility of the stepping curve when a scattering object is inserted in the beam. For homogeneous specimens that show no or negligible small-angle scattering, the dark-field signal (relative visibility V) is close to unity, whereas strong scattering samples yield dark-field signals of $V < 1$.

The relative visibility is directly related to small-angle scattering and multiple refraction from microstructures with a scale much smaller than the spatial resolution of the imaging system (24, 27). This signal reveals structural information on the nanometer to hundreds-of-micrometers scale that is inaccessible from both the absorption and the phase-contrast image (28, 29). Biomedical applications of dark-field contrast include bone imaging (30, 31), calcifications in breast imaging (32), and tooth imaging (33).

In this paper, we use strong small-angle scattering from mouse lungs in grating-based dark-field imaging. The distinct dependency of the dark-field signal on mean alveolar size leads to improved diagnosis of emphysema in single projections.

Results

Three emphysematous and three healthy mouse lung samples were measured with a two-grating interferometer setup (Fig. 1 *A* and *B*). The measurements were performed at 36 keV using a monochromatic laser-driven miniature synchrotron X-ray source [Compact Light Source (CLS)] (Fig. 1*C*). Multiple raw projections are acquired during a phase-stepping scan of the absorption grating with respect to the phase grating (Fig. 1*E*). The effect of the sample on the wavefront is then calculated using Fourier analysis, resulting in three different contrast modalities (34): standard absorption, phase-contrast, and dark-field images. Fig. 2 *Top* displays all six mouse lungs measured in the experiment; below, a control (blue) and one emphysematous (red) lung is displayed in all three contrast modalities, respectively. Image contrast is adjusted to give maximum detail readability. In a comparison of the absorption images, the anticipated transmission increase in the emphysema lung is clearly visible. The clear depiction of the lung in the dark-field signal can be attributed to strong small-angle scattering of X-rays originating from air-filled alveolar structures of the fixated lung.

To yield better emphysema diagnosis, we propose combining both transmission and scattering information of the samples in a single scatter plot (Fig. 3). Each point in the scatter plot represents transmission and dark-field pixel values of a lung projection. The data of all six lungs are presented, measured in 11 projections each. The emphysematous lung (red) shows increased transmission with respect to water and reduced scattering, and the healthy lung tissue (blue) shows less increase in transmission and more scattering than the emphysema lung. In this multimodal visualization, a clear separation of healthy vs. diseased tissue is achieved (Fig. 3).

Our findings are in good agreement with both theoretical and experimental models, where microspheres of well-defined sizes have been used to simulate lung tissue (15). Wave-optical X-ray propagation simulations of 33-keV X-rays through a mouse lung model with average alveolar size of 60 μm yielded an average deflection angle of zero degrees with a SD of 11 μrad (15). The sensitivity of the grating interferometer can be tuned to specific scattering angles by adjusting the inter-grating distance and absorption grating period (35). From the geometrical parameters of our experimental setup we can expect a large decrease in visibility for diffraction angles in the range of $p_2/d = 13.6$ μrad (28), which matches the simulated angular spread well and accounts for the large decrease in visibility apparent in the lung projection measurements (Fig. 2).

The influence of sample structural parameters on the visibility has been simulated in Malecki et al. (36) and can, in the case of randomly distributed spheres of known radius, be calculated analytically (35). We consider a lung model of air-filled spheres embedded in a lung tissue matrix with a fixed-sphere volume fraction and increasing sphere radius (as depicted in

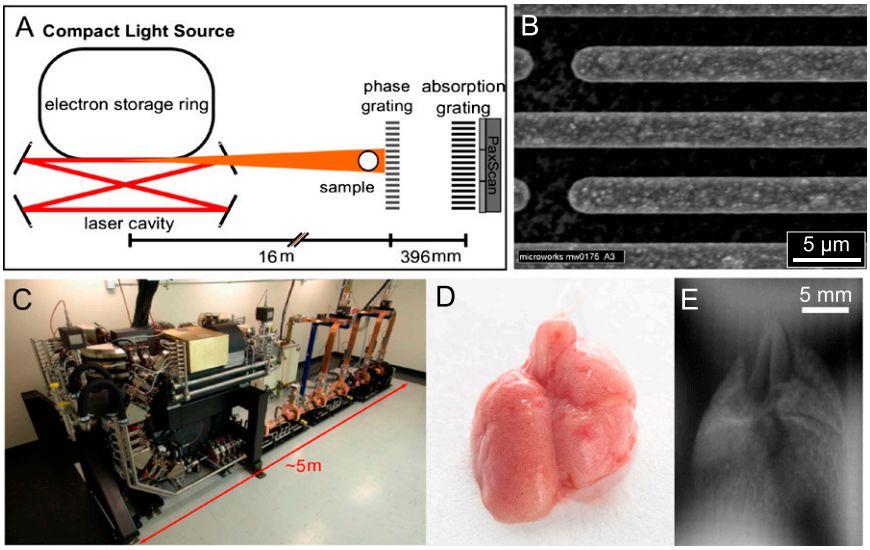

Fig. 1. The CLS consists of an electron storage ring combined with a high-finesse laser cavity. At the interaction point of the counter propagating electron bunch and laser pulse, hard X-rays are produced in the process of inverse Compton scattering. (*A*) The grating interferometer comprises a phase grating, an absorption grating, and a Varian PaxScan detector. (*B*) SEM image of the phase gratings with a periodicity of $P = 5.275$ μm. (*C*) CLS showing the linear accelerator section and the electron storage ring. (*D*) The mouse lungs were inflated with air and tied up at the trachea after excision. (*E*) Raw projection image of the formalin-fixated mouse lung measured in a water bath.

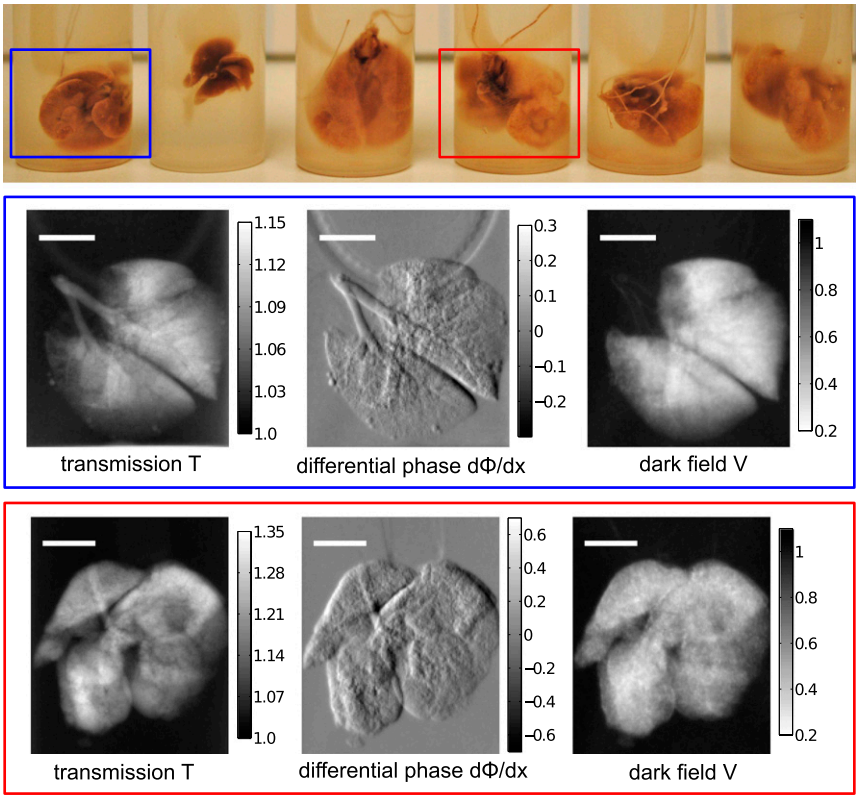

Fig. 2. Three elastase and three control mouse lungs were included in the study. The picture shows all six mouse lungs in formalin-filled plastic cylinders. The blue (healthy lung) and red (emphysematous lung) rectangle indicates the samples that are displayed in transmission *T* with respect to water, differential phase *dΦ/dx*, and dark-field *V* below. (Scale bars: 5 mm.)

the sketch next to the scatter plot; Fig. 3): The transmission through all samples with identical sphere volume fraction will stay constant. The change in dark-field signal with increasing sphere radius can be calculated using equations 25 and 26 in ref. 35, assuming an electron density difference of $\Delta\rho_e = 3.4997 \times 10^2\ \mathrm{nm}^{-3}$ (16), a constant volume fraction of 0.5, and a sample thickness of 7 mm. A change in sphere diameter from 80 μm, corresponding to the mean alveoli diameter in healthy mice (37), to 90 μm results in a 25% visibility increase from $V = 0.12$ to $V = 0.15$. We conclude that subtle changes in alveoli diameter during early stages of emphysema are likely to appear in the dark-field image without any significant signature in absorption contrast.

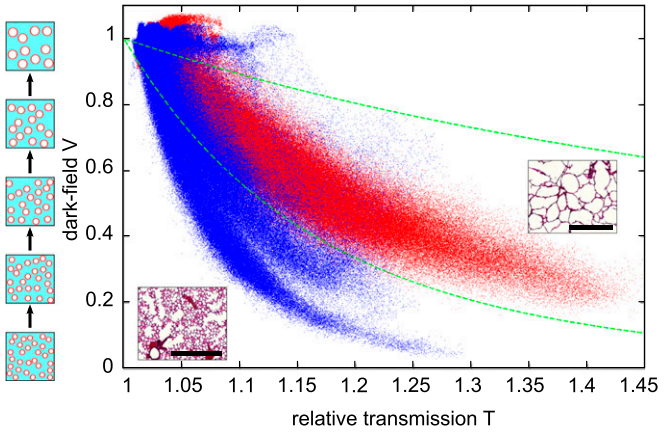

Fig. 3. Scatter plot of dark-field *V* vs. transmission relative to water *T* of all six lung radiographs and the data from 11 projection angles. From this statistical analysis a clear distinction between emphysematous (red) and control (blue) lung tissue is possible. Two green dotted curves represent a fixed ratio of the logarithm of dark-field contrast and transmission values ln(*V*)/ln(*T*). Pixels in between these curves are used for further image analysis in Fig. 6. (*Insets*) Histological sections in 10-fold magnification. (Scale bars: 500 μm.)

Experimental data from dark-field phantom measurements using polymethylmethacrylate (PMMA) and glass microspheres support both our interpretation of the lung-imaging results and the described analytical model. In the measurements the dark-field signal V decreased with increasing microsphere diameters in the range from 2.5 μm to 600 μm (35, 38).

The change in alveoli diameter is well represented in the histological sections of healthy (Fig. 4 *A* and *B*) and emphysematous lung samples (Fig. 4 *C* and *D*), where the loss in lung tissue accompanied by a significant increase in mean alveolar diameter is apparent in the 10-fold magnification of emphysematous mouse lung tissue (Fig. 4*D*). Clinically relevant parameters of pulmonary function were tested, and values for dynamic compliance and tissue elastance are given in Fig. 5 and Table 1. The increase in dynamic compliance due to the loss of alveolar and elastic tissue associated with emphysema can be observed. Furthermore, lung function in mice treated with elastase demonstrated a decrease in tissue elastance (37, 39). The functional pattern of the mouse respiratory disease model is thus closely related to emphysema in humans.

The apparent discrimination of healthy and emphysematous lung tissue in the scatter plot (Fig. 3) can be visualized in lung projection images by selecting the pixels of emphysematous tissue that show a large deviation from the healthy (blue) curve. The slope of linear curves fitted to scatter plots of the logarithm of dark-field, ln(*V*), and transmission value, ln(*T*), of each lung sample is higher for emphysematous lungs (-4.8 ± 0.2) than for healthy lungs (-10.6 ± 3.4). Threshold values of ln(*V*)/ln(*T*) have been set to a cutoff value of −6 to distinguish emphysematous from healthy lung tissue and −1.2 to exclude background pixel values (dotted green lines in Fig. 3). Scatter plot data points inside these limits have been plotted with their ln(*V*)/ln(*T*) value overlaid on conventional absorption projections in Fig. 6. This multimodal visualization leads to a pronounced difference

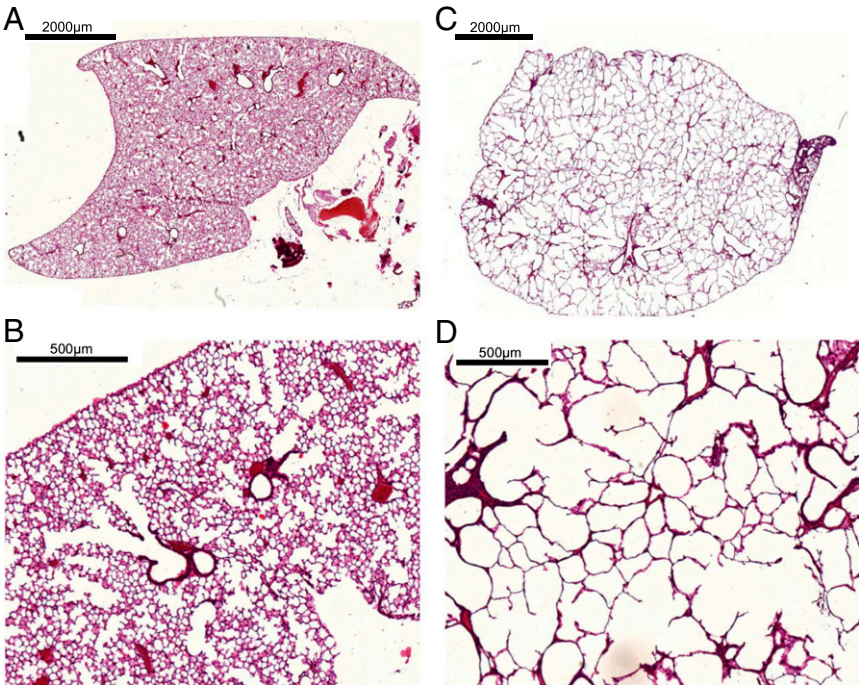

Fig. 4. Histological sections of lung structure in experimental emphysema. Lung samples were embedded in paraffin and stained using a routine Mayer's H&E staining protocol. (*A* and *C*) 2× and (*B* and *D*) 10× magnification of the lung sections, respectively. In the control group (*A* and *B*), a dense alveolar network is nicely visible, whereas the emphysema lung (*C* and *D*) displays the expected pathological larger alveoli diameters with a reduced alveoli number.

between the three emphysematous and three control lung samples in single projections. Standard absorption contrast is depicted in the linear gray scale with relative transmission values (with respect to water) ranging from 1 to 1.35, whereas $\ln(V)/\ln(T)$ is displayed in jet colors ranging from −6 to −1.2, where high values (yellow, red) correspond to lower scattering from the sample at comparable absorption properties, thus revealing larger mean alveoli diameter. The quotient $\ln(V)/\ln(T)$ can be expressed in terms of material-dependent parameters, namely the linear diffusion coefficient ε and the linear attenuation coefficient μ (28):

$$\frac{\ln(V)}{\ln(T)} \propto \frac{\int \varepsilon(z)\mathrm{d}z}{\int \mu(z)\mathrm{d}z}. \qquad [1]$$

Because the lung was measured with respect to water, the denominator $\ln(T)$ is proportional to the thickness of the lung, e.g., thickness of air the beam crosses, whereas $\ln(V)$ decreases with increased scattering from the sample. The quantity $\ln(V)/\ln(T)$ thus combines the information from single absorption and dark-field images. Assuming similar transmission through emphysematous and healthy lung tissue, each pixel's value of $\ln(V)/\ln(T)$ is proportional to the mean linear diffusion coefficient ε along lung tissue crossed by the X-ray beam, where ε strongly depends on the size of the scattering microstructure. In a less severe case of emphysema this visualization could help identifying small regions of affected lung tissue in single projections.

To investigate whether this imaging approach is also feasible in the in situ setting, we performed an additional experiment with an intact mouse imaged postmortem. Fig. S1 shows how the strong dark-field signal from the lung is preserved through overlying ribs, spine, skin, and fur.

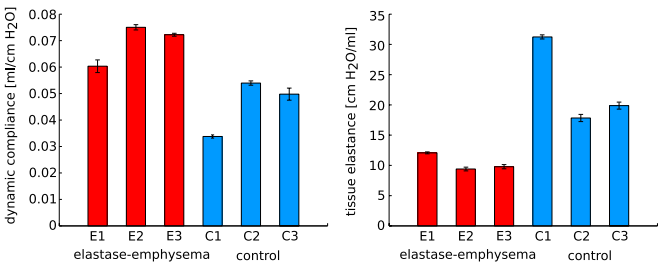

Fig. 5. Pulmonary function of six mice included in the experiment. For all samples, dynamic compliance and tissue elastance with their respective SD are depicted. In a comparison of control (blue) and elastase-induced emphysema (red) samples, the expected increase in dynamic compliance and reduction in tissue elastance is apparent. Values are given in Table 1.

Discussion

The change in X-ray attenuation caused by the pathological process of pulmonary emphysema is difficult to detect in early stage of the disease using conventional absorption-based radiography. In this paper we present grating-based dark-field images of emphysematous vs. healthy lung tissue. A combination of absorption and dark-field signal in a scatter-plot analysis demonstrates improved emphysema diagnosis in single projections of mice lungs. Strong dependence of the dark-field signal on structural changes in the alveolar network has been established.

Further investigations will aim at transferring the proposed analysis from isolated lung samples, measured in a water bath, to lung imaging in mice. An ex vivo dark-field image of an inflated lung in a mouse (Fig. S1) shows that the strong dark-field signal from the lung is not significantly degraded by the overlying structures such as the ribs and the spine. Furthermore, it has been demonstrated by Kitchen et al. (40) that the projected thickness of bone and soft tissue can be extracted from a single differential phase and absorption projection image of a mouse. These values can be used to normalize both transmission T and dark-field V before an analysis of projected lung diffusion coefficient ε.

In addition to a decrease in pulmonary function of emphysematous mice, which was evident from dynamic compliance and tissue elastance measurements, the emphysematous microstructure of the lung samples was confirmed by histology, where an enlargement of airspaces accompanied by the destruction of their walls is clearly visible. The functional defects present in the mouse respiratory disease model are thus closely related to emphysema in humans.

The distinct signature of the elastase-induced emphysema mice in lung function measurements is attributed to the advanced stage of the disease and is expected to break down for

Table 1. Lung function measurements

Lung sample	Dynamic compliance, mL/cmH_2O	Tissue elastance, cmH_2O/mL
Elastase emphysema 1	0.0603 ± 0.0022	12.072 ± 0.064
Elastase emphysema 2	0.0750 ± 0.0009	9.400 ± 0.261
Elastase emphysema 3	0.0722 ± 0.0005	9.781 ± 0.299
Control 1	0.0338 ± 0.0005	31.239 ± 0.296
Control 2	0.0540 ± 0.0007	17.835 ± 0.548
Control 3	0.0498 ± 0.0022	19.88 ± 0.539

subtle changes in lung tissue during early stages of emphysema. Detailed studies looking at different stages and regional distributions of emphysema are planned to assess the potential of our method for emphysema staging and its prospect to replace invasive histopathology.

The dose of 33.9 mGy used in our experiment is significantly higher than the surface dose of 0.25 mGy used in a conventional clinical chest radiograph (41). A reduction of the number of phase steps and binning, simulating a reduced exposure time and larger pixel size, yielded low-dose dark-field results, which are comparable to the oversampled dataset (Fig. S2). Furthermore, the surface dose can be significantly reduced through an optimization of the experimental setup—namely, thinning of the grating wafers (which currently comprise 1 mm of silicon), optimization of grating design energy, and an overall increase in X-ray energy. Shorter exposure times can be achieved by using single-shot Moiré techniques (42, 43), where image resolution is reduced, while the sensitivity of the dark-field signal to changes in lung structure is not altered.

This proof-of-principle synchrotron-based experiment was conducted at the CLS using highly brilliant and monochromatic X-rays to achieve the benchmark results presented here. Future work will focus on establishing the applicability of the method to higher X-ray energies, as necessary for human chest radiographs, and with conventional X-ray tubes, where grating-based phase-contrast imaging has already been successfully demonstrated. With these improvements, we expect our approach of combined dark-field and absorption contrast X-ray imaging to offer the possibility of early-stage emphysema detection in humans and assess its regional distribution without the use of CT.

Materials and Methods

Compact Light Source. CLS is a laboratory-scale synchrotron X-ray source, commercially developed and manufactured by Lyncean Technologies, Inc. A radiofrequency electron gun and a laser-driven photocathode produce single-electron bunches, which are accelerated to an energy in the range of 20–45 MeV in a linear electron accelerator section. The bunch is stored at this energy in a miniature storage ring with a circumference of a few meters (Fig. 1*C*). A high-finesse bow-tie enhancement cavity is located at one of the straight sections of the storage ring and is resonantly driven by an infrared laser. At the interaction point, the laser and the electron bunch are tightly focused and pass through each other on each revolution of the electron bunch and each cycle of the laser pulse. Through the process of inverse Compton scattering, pulses of X-rays are produced on each revolution (44). Let λ_L and γ denote laser wavelength and electron energy given in units of rest mass, respectively. The emitted spectrum is similar to that of a long magnetic undulator with the fundamental wavelength of the laser undulator being $\lambda_L/4\gamma^2$ (45). Tight focusing of both the electron bunch and the infrared laser results in high flux and a small source size of 40 × 40 μm^2 rms. The high degree of spatial coherence can be exploited in the straightforward use of refraction-based imaging techniques (46, 47), and the intrinsic energy bandwidth of $\Delta E/E_{peak} = 3\%$ allows for monochromatic biomedical imaging experiments. The angular divergence of about 4 mrad is larger than at conventional synchrotron sources and provides a circular field of view of about 6 cm at a distance of 16 m from the source, which can be used to measure relatively large biological samples.

Grating Interferometer. A grating interferometer was placed 16 m from the source. A $\pi/2$ phase-shift grating with 5.28-μm pitch (design energy 33 keV) and an absorption grating with 5.4-μm pitch were used at the first fractional Talbot distance (Fig. 1 *A* and *B*). CLS was operated at an X-ray energy of E_{peak} = 36 keV (λ_{peak} = 0.34 Å), with a full energy spread of $\Delta E/E_{peak} = 3\%$. Each dataset consists of a phase-stepping scan of the absorption grating with respect to the phase grating, over one grating period using 16 steps. The exposure time for each phase step was 5 s. To increase statistics and ensure independency from sample alignment with respect to the interferometer orientation, lungs from six different mice were rotated around a tomographic axis recording 11 projections over 180°. All images were recorded using a Varian PaxScan 2520D detector with square pixels of 127 × 127 μm^2 and a CsI scintillator. To account for small X-ray intensity variations, a scintillation detector was placed close to the source, monitoring X-rays scattered from a Kapton foil. The surface entrance dose was calculated based on the measured flux density 8 × 10^6 photons s^{-1}·mm^{-2} at 36 keV and the known absorption coefficient of dry air. Including all phase steps with 5 s exposure time each, the surface entrance dose of one projection is 33.9 mGy.

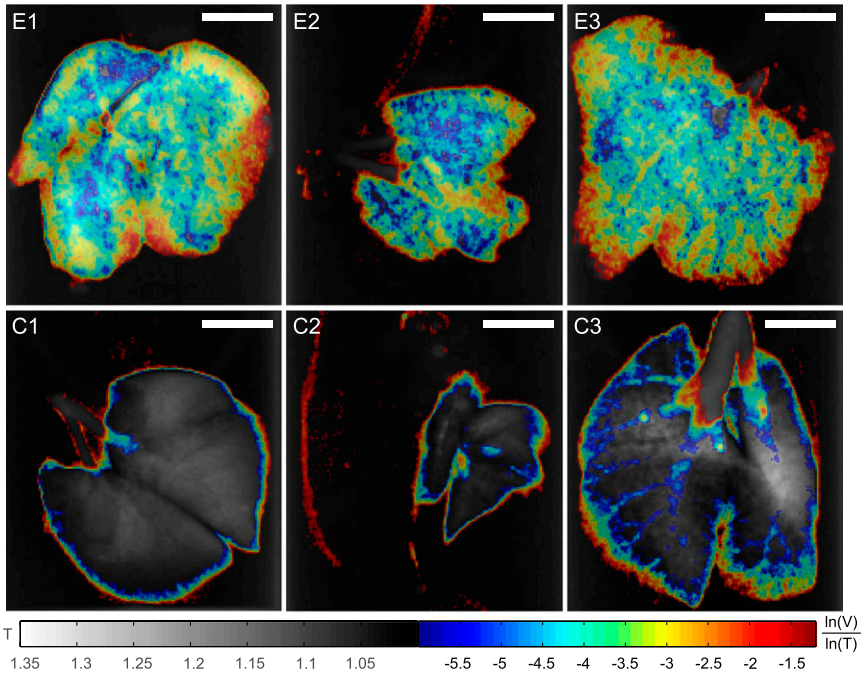

Fig. 6. Multimodal projections of three emphysematous lung samples (E1, E2, E3) and three control lung samples (C1, C2, C3). To visualize the apparent differentiation of healthy and emphysematous lungs from the scatter plot (Fig. 3), we propose using threshold values on the quotient of the logarithm of dark-field contrast and transmission values $\ln(V)/\ln(T) = -6$ and $\ln(V)/\ln(T) = -1.2$ (dotted green lines in Fig. 3). In single projections, the corresponding pixels have been superimposed on the conventional transmission contrast image with their color representing $\ln(V)/\ln(T)$. Standard transmission is depicted in the linear gray scale with transmission values (with respect to water) ranging from 1 to 1.35. The material-dependent quotient $\ln(V)/\ln(T)$ is displayed in jet colors ranging from −6 to −1.2, where higher values (yellow, red) correspond to lower scattering at similar transmission and thus larger mean alveoli diameter. (Scale bars: 5 mm.)

The dose level of this first in vitro study was not optimized and can be significantly decreased [e.g., by reducing the support thickness of the grating structures (factor 0.8), by reducing the exposure time (factor 0.25), or by using four instead of 16 phase-steps (factor 0.25)].

Experimental Emphysema in Mice. Six- to 8-wk-old pathogen-free female C57BL/6N mice (Charles River Laboratories) were used throughout this study. Mice had free access to water and rodent laboratory chow. Pancreatic elastase was dissolved in sterile PBS and applied orotracheally (80 U/kg body weight). Control mice received 80 μL sterile PBS. All animal experiments were carried out in strict accordance with the recommendations in the Guide for the Care and Use of Laboratory Animals of the National Institutes of Health. The protocol was approved by the ethical committee of the regional governmental commission of animal protection (Munich).

To assess information on pulmonary function, the mice were anesthetized, tracheostomized, and connected to a Scireq flexiVent pulmonary function system (EMKA Technologies). During the measurement, mice were ventilated with an average breathing frequency of 160/min. After a maximal vital capacity perturbation (total lung capacity), a snapshot perturbation maneuver was applied to determine the dynamic compliance of the whole respiratory system according to the single compartment model. Then the forced oscillation technique perturbation maneuvers quick primewave-3 and primewave-8 were conducted, resulting in tissue elastance. For each parameter, an average of three measurements per mouse was calculated and depicted. Mouse lungs were excised 28 d after elastase application, inflated with air, and tied up at the trachea (48) (Fig. 1*C*). The samples were put in formalin-filled plastic containers (Fig. 2) and measured in a water bath.

Histology. After washing to remove paraformaldehyde, lungs were decalcified in 10% (wt/vol) EDTA in H_2O for 5 d. Subsequently, the specimens were dehydrated and embedded in paraffin. Multiple 10-μm thin sections were prepared in the coronal plane at intervals of 0.5 mm to obtain representative sections covering the entire organ. Sections were deparaffinized, hydrated, stained using a routine Mayer's H&E staining protocol, and dehydrated. Sections were scanned at various magnifications to create digital images.

ACKNOWLEDGMENTS. We thank J. Hostens, B. Pauwels, A. Velroyen, and A. Yaroshenko for providing ex vivo mouse projection images. Support for this work was provided by the Deutsche Forschungsgemeinschaft Cluster of Excellence Munich Center for Advanced Photonics and European Research Council Seventh Framework Programme Starting Grant 240142 (to S.S., F.G.M., M.B., J.H., K.A., G.P., A.M., S.A.-N., and F.P.). This work was partly carried out with the support of the Karlsruhe Nano Micro Facility (KNMF; www.kit.edu/knmf), a Helmholtz Research Infrastructure at Karlsruhe Institute of Technology (KIT; www.kit.edu). The Compact Light Source experiment was supported in part by National Institute of General Medical Sciences Grant R44-GM074437 and National Center for Research Resources Grant R43-RR025730. S.S. and A.M. acknowledge the Technische Universität München Graduate School for the support of their studies.

1. Zvezdin B, et al. (2009) A postmortem analysis of major causes of early death in patients hospitalized with COPD exacerbation. *Chest* 136(2):376–380.
2. Celli BR, MacNee W ATS/ERS Task Force (2004) Standards for the diagnosis and treatment of patients with COPD: A summary of the ATS/ERS position paper. *Eur Respir J* 23 (6):932–946.
3. Minai OA, Benditt J, Martinez FJ (2008) Natural history of emphysema. *Proc Am Thorac Soc* 5(4):468–474.
4. Ley-Zaporozhan J, Ley S, Kauczor HU (2008) Morphological and functional imaging in COPD with CT and MRI: Present and future. *Eur Radiol* 18(3):510–521.
5. Washko GR (2010) Diagnostic imaging in COPD. *Semin Respir Crit Care Med* 31(3): 276–285.
6. Soriano JB, Zielinski J, Price D (2009) Screening for and early detection of chronic obstructive pulmonary disease. *Lancet* 374(9691):721–732.
7. Sciurba FC, et al. (2010) A randomized study of endobronchial valves for advanced emphysema. *N Engl J Med* 363(13):1233–1244.
8. Criner GJ, Mamary AJ (2010) Lung volume reduction surgery and lung volume reduction in advanced emphysema: Who and why? *Semin Respir Crit Care Med* 31(3): 348–364.
9. Hooper SB, et al. (2007) Imaging lung aeration and lung liquid clearance at birth. *FASEB J* 21(12):3329–3337.
10. Parsons DW, et al. (2008) High-resolution visualization of airspace structures in intact mice via synchrotron phase-contrast X-ray imaging (PCXI). *J Anat* 213(2):217–227.
11. Kitchen MJ, et al. (2005) Phase contrast X-ray imaging of mice and rabbit lungs: A comparative study. *Br J Radiol* 78(935):1018–1027.
12. Connor DM, et al. (2011) Diffraction enhanced imaging of a rat model of gastric acid aspiration pneumonitis. *Acad Radiol* 18(12):1515–1521.
13. Zhang L, Li D, Luo S (2011) Non-invasive microstructure and morphology investigation of the mouse lung: Qualitative description and quantitative measurement. *PLoS ONE* 6(2):e17400.
14. Jheon S, Youn HS, Kim HT, Choi GH, Kim JK (2006) High-resolution X-ray refraction imaging of rat lung and histological correlations. *Microsc Res Tech* 69(8):656–659.
15. Kitchen MJ, et al. (2004) On the origin of speckle in x-ray phase contrast images of lung tissue. *Phys Med Biol* 49(18):4335–4348.
16. Kitchen MJ, Paganin D, Lewis RA, Yagi N, Uesugi K (2005) Analysis of speckle patterns in phase-contrast images of lung tissue. *Nucl Instrum Methods Phys Res A* 548:240–246.
17. Khelashvili G, et al. (2006) A physical model of multiple-image radiography. *Phys Med Biol* 51(2):221–236.
18. Rigon L, Arfelli F, Menk R (2007) Three-image diffraction enhanced imaging algorithm to extract absorption, refraction and ultrasmall-angle scattering. *Appl Phys Lett* 90(11):114102–114105.
19. Kitchen MJ, et al. (2010) X-ray phase, absorption and scatter retrieval using two or more phase contrast images. *Opt Express* 18(19):19994–20012.
20. Zhong Z, Thomlinson W, Chapman D, Sayers D (2000) Implementation of diffraction-enhanced imaging experiments: At the NSLS and APS. *Nucl Instrum Methods Phys Res A* 450:556–567.
21. Parham C, Zhong Z, Connor DM, Chapman LD, Pisano ED (2009) Design and implementation of a compact low-dose diffraction enhanced medical imaging system. *Acad Radiol* 16(8):911–917.
22. Nesch I, et al. (2009) The design and application of an in-laboratory diffraction-enhanced x-ray imaging instrument. *Rev Sci Instrum* 80(9):093702.
23. Pfeiffer F, et al. (2007) High-resolution brain tumor visualization using three-dimensional x-ray phase contrast tomography. *Phys Med Biol* 52(23):6923–6930.
24. Pfeiffer F, et al. (2008) Hard-X-ray dark-field imaging using a grating interferometer. *Nat Mater* 7(2):134–137.
25. Weitkamp T, et al. (2005) X-ray phase imaging with a grating interferometer. *Opt Express* 13(16):6296–6304.
26. Momose A, et al. (2003) Demonstration of X-ray Talbot interferometry. *Jpn J Appl Phys* 42:L866–L868.
27. Bech M, et al. (2012) Experimental validation of image contrast correlation between ultra-small-angle X-ray scattering and grating-based dark-field imaging using a laser-driven compact X-ray source. *Photonic Laser Med* 1(1):47–50.
28. Bech M, et al. (2010) Quantitative x-ray dark-field computed tomography. *Phys Med Biol* 55(18):5529–5539.
29. Chen GH, Bevins N, Zambelli J, Qi Z (2010) Small-angle scattering computed tomography (SAS-CT) using a Talbot-Lau interferometer and a rotating anode x-ray tube: Theory and experiments. *Opt Express* 18(12):12960–12970.
30. Potdevin G, et al. (2012) X-ray vector radiography for bone micro-architecture diagnostics. *Phys Med Biol* 57(11):3451–3461.
31. Wen H, Bennett EE, Hegedus MM, Rapacchi S (2009) Fourier X-ray scattering radiography yields bone structural information. *Radiology* 251(3):910–918.
32. Momose A, et al. (2005) Attempt at visualizing breast cancer with X-ray dark field imaging. *Jpn J Appl Phys* 44:528–531.
33. Jensen TH, et al. (2010) Directional x-ray dark-field imaging of strongly ordered systems. *Phys Rev B* 82:214103.
34. Pfeiffer F, et al. (2009) X-ray dark-field and phase-contrast imaging using a grating. interferometer. *J Appl Phys* 105:102006.
35. Yashiro W, Terui Y, Kawabata K, Momose A (2010) On the origin of visibility contrast in x-ray Talbot interferometry. *Opt Express* 18(16):16890–16901.
36. Malecki A, Potdevin G, Pfeiffer F (2012) Quantitative wave-optical numerical analysis of the dark-field signal in grating-based x-ray interferometry. *Europhys Lett* 99(4):48001.
37. Irvin CG, Bates JH (2003) Measuring the lung function in the mouse: The challenge of size. *Respir Res* 4(1):4.
38. Miller EA, White TA, McDonald BS, Seifert A, Flynn M (2010) Phase contrast x-ray imaging signatures for homeland security applications. *Nuclear Science Symposium Conference Record, 2010 IEEE* (Inst Elec Electr Eng, New York), pp 896–899.
39. Vanoirbeek JAJ, et al. (2010) Noninvasive and invasive pulmonary function in mouse models of obstructive and restrictive respiratory diseases. *Am J Respir Cell Mol Biol* 42 (1):96–104.
40. Kitchen MJ, et al. (2011) Phase contrast image segmentation using a Laue analyser crystal. *Phys Med Biol* 56(3):515–534.
41. Gray JE, et al. (2005) Reference values for diagnostic radiology: Application and impact. *Radiology* 235(2):354–358.
42. Takeda M, Ina H, Kobayashi S (1982) Fourier-transform method of fringe-pattern analysis for computer-based topography and interferometry. *J Opt Soc Am* 72(1): 156–160.
43. Momose A, Yashiro W, Maikusa H, Takeda Y (2009) High-speed X-ray phase imaging and X-ray phase tomography with Talbot interferometer and white synchrotron radiation. *Opt Express* 17(15):12540–12545.
44. Huang Z, Ruth RD (1998) Laser-electron storage ring. *Phys Rev Lett* 80(5):976–979.
45. Loewen R (2003) A Compact Light Source: Design and technical feasibility study of a laser-electron storage ring x-ray source. PhD dissertation SLAC-R-632 (Stanford Univ, Stanford, CA).
46. Bech M, et al. (2009) Hard X-ray phase-contrast imaging with the Compact Light Source based on inverse Compton X-rays. *J Synchrotron Radiat* 16(Pt 1):43–47.
47. Schleede S, et al. (2012) Multimodal hard X-ray imaging of a mammography phantom at a compact synchrotron light source. *J Synchrotron Radiat* 19(Pt 4):525–529.
48. Kneidinger N, et al. (2011) Activation of the WNT/β-catenin pathway attenuates experimental emphysema. *Am J Respir Crit Care Med* 183(6):723–733.